Pacific Northwest
NATIONAL LABORATORY

PNNL-30487

Improving Ductility of Hydride Embrittled Zirconium

August 2020

Jake L Bair
David G Abrecht
Nicole R Overman
Anthony D Guzman
David A Collins
Richard M Cox
Shawn L Riechers

U.S. DEPARTMENT OF ENERGY

Prepared for the U.S. Department of Energy
under Contract DE-AC05-76RL01830

DISCLAIMER

PACIFIC NORTHWEST NATIONAL LABORATORY
operated by
BATTELLE
for the
UNITED STATES DEPARTMENT OF ENERGY
under Contract DE-AC05-76RL01830

Printed in the United States of America

Available to DOE and DOE contractors from the
Office of Scientific and Technical Information,
P.O. Box 62, Oak Ridge, TN 37831-0062;
ph: (865) 576-8401
fax: (865) 576-5728
email: reports@adonis.osti.gov

Available to the public from the National Technical Information Service
5301 Shawnee Rd., Alexandria, VA 22312
ph: (800) 553-NTIS (6847)
email: orders@ntis.gov <https://www.ntis.gov/about>
Online ordering: http://www.ntis.gov

PNNL-30487

Improving Ductility of Hydride Embrittled Zirconium

Final Report

August 2020

Jake L Bair
David G Abrecht
Nicole R Overman
Anthony D Guzman
David A Collins
Richard M Cox
Shawn L Riechers

Prepared for
the U.S. Department of Energy
under Contract DE-AC05-76RL01830

Pacific Northwest National Laboratory
Richland, Washington 99354

Abstract

One of the main limiting factors on the lifetimes of nuclear fuel rod claddings is the formation of hydrides and associated detrimental effects on mechanical properties. In this study, we examined the behavior of hydrides in zirconium and zircaloy-4 after tensile stress is applied to determine whether the more ductile γ-ZrH phase was stabilized by the mechanical stress. We did not find a significant increase in the ratio of γ-ZrH phase to δ-$ZrH_{1.5}$ phases after tensile stress is applied in previously hydrided metals. Previous reports indicate that this stabilization does occur when zircaloy is stressed and hydrided simultaneously, indicating that the formation of the γ-ZrH phase may reverse upon relaxation or may require the stress in-situ during the hydriding process to form in significant quantities.

Acknowledgments

This project was funded by Pacific Northwest National Laboratory's Laboratory Directed Research and Development Funds. Pacific Northwest National Laboratory is operated by Battelle Memorial Institute for the U. S. Department of Energy under contract number DE-AC05-76RL01830.

Acronyms and Abbreviations

AFM	atomic force microscopy
at%	atomic percentage
CMOS	complementary metal-oxide-semiconductor
EBSD	electron backscatter diffraction
eV	electron volt
GP	grand potential
GPa	gigapascal (10^9 pascals)
HF	hydrofluoric acid
HNO_3	nitric acid
Hz	hertz (1 per second)
kV	kilovolt (10^3 volts)
m	meter
mJ	milliJoule (10^{-3} Joules)
mm	millimeter (10^{-3} meters)
MPa	megapascal (10^6 pascals)
N/m	Newtons per meter
nm	nanometer (10^{-9} meters)
o.d.	outer diameter
PFM	phase field model
ppm	parts per million
SEM	scanning electron microscopy
µm	micrometer (10^{-6} meters)
µN	micronewtons (10^{-6} newtons)
V	volt
Zr	zirconium
Zr_xH_y	zirconium hydride (x and y as numbers representing different ratios)

Contents

Figures

Tables

1.0 Introduction

Hydride embrittlement is a common problem in many metals such as magnesium, tantalum, zirconium, niobium, and others [Bair 2015]. Hydrogen can enter materials from an uncontrolled atmosphere during heat treatments, corrosion processes, welding, casting, or be inserted purposefully for hydrogen storage. Stresses in the metal increase hydride formation at crack tips, leading to further crack propagation and failure. In some of these reactive metals, several hydride phases can form of varying ductility and brittleness. If treatments are found which can stabilize only the most ductile hydride phases, the embrittlement and cracking problems seen in these materials could be significantly reduced.

1.1 Background

Zirconium-based alloys are commonly used in nuclear fuel rod claddings due to excellent radiation properties combined with decent mechanical properties and corrosion resistance [Bair 2015, Ells 1968, Cox 1990, Ensor 2017, Chernov 2017]. One of the main limiting factors on the lifetimes of these claddings is the formation of hydrides and associated detrimental effects on mechanical properties. Water used to cool the claddings dissociates into hydrogen and oxygen. The oxygen forms an oxide layer on the outside of the cladding, freeing the hydrogen to diffuse into the bulk where it reacts to form brittle hydrides. The most common phase of hydrides is $\delta{-}ZrH_{1.5}$, but several works indicate that the metastable $\zeta{-}Zr_2H$ and $\gamma{-}ZrH$ phases may form as precursors to the stable δ phase [Bair 2016, Zhang 2017]. A 2010 study by Zhu et al showed that the metastable ζ and γ phases are significantly more ductile than the δ phase [Zhu 2010]. It may significantly reduce the problems seen in claddings with embrittlement if the more ductile phases can take the place of the δ phase. Recent in situ studies indicate that one or both of these metastable phases can be stabilized by mechanical stress or temperature treatments [Wang 2016, Li 2017]. Wang et al found that a slow cooling rate could cause a phase transformation from δ to γ [Wang 2016], and Li et al found a deformation induced transformation from δ to ζ with a threshold stress of 370 MPa at room temperature [Li 2017]. The elastic properties of all three phases indicate that the free energy of δ would increase more under elastic stresses than the other two phases. This could explain why one of the metastable phases could become stable under certain deformation conditions. In this work, we attempted to find a method to stabilize the metastable γ phase using a variety of stress and temperature treatments. A simple phase field model was also used to determine a theoretical stress for phase stability.

2.0 Methods

This study comprised both experimental and computational approaches to investigating the behavior of zirconium and zircaloy hydrides. Computational techniques primarily comprised the use of phase field modeling (PFM) to describe the dynamic behavior of zirconium alloys under stress. Experimental techniques comprised the apparatus used to create hydrides and to test their mechanical properties, as well as the use of multiple forms of microscopy to study the behaviors of grain transformation. Details of the techniques are described in the following sections.

2.1 Zirconium hydriding

Zirconium metal alloy sheets (Grade ZR702, 99.2% Zr/Hf, 4.5% Hf maximum) were acquired from Eagle Alloys. The procured sheets had dimensions of 0.050 inches thick x 12 inches x 24 inches. Zircalloy-4 (Grade R60804, 98% Zr, 1.5% Sn, 0.5% Fe/Cr) was obtained from American Elements with similar dimensions. Tensile specimen dogbones were cut from the metal sheets. The dimensions for the dogbones are displayed in Figure 2-1.

Specimens were hydrided in a vacuum apparatus heated by a clamshell resistive heating furnace. The specimen was held in a quartz crucible that was placed within a one-inch o.d. glass furnace tube. The furnace tube inserts into the clamshell heater and holds the specimen in the middle of a four-inch heat zone. Prior to loading the sample with hydrogen, it is heated to 580 °C as measured externally within the heat zone by a Type K thermocouple for two hours under vacuum at 10^{-7} Torr. The specimen is subsequently cooled to room temperature and stored under vacuum until loading.

In order to optimize the hydriding procedure for these specimens, a wide variety of techniques were utilized and evaluated. The study outlined in Li et al. [Li 2017] utilized a baseline of 600 ppm hydrogen by weight to evaluate the effects of mechanical deformation on the $\delta - \zeta$ phase transformation. However, that study did not specify the hydriding technique utilized, so the optimal hydriding technique had to be developed independently. In addition to the nominal 600 ppm hydrogen loading, the effects of a nominal 6000 ppm loading were explored. Although reaching these nominal loadings were difficult due to inherent subtleties in the hydriding apparatus compared to the one in Li et al. [Li 2017], as long as the concentration was within 2.5% it was assumed that the data acquired would be sufficient to extrapolate the behavior at the nominal hydrogen loading.

The specimen is loaded in one of two ways. The first is to introduce a small amount of hydrogen equivalent to the required moles for the target loading (~600 ppm by weight). The specimen is then heated to ~620 °C and the pressure decrease measured by an MKS Baratron monitored until equilibrium is reached. Heating is then discontinued, the specimen is cooled slowly to room temperature, and the remaining hydrogen evacuated. Subsequently, a slight positive pressure of helium (~800 Torr) is introduced into the system until the specimen is retrieved. Alternatively, ~700 Torr of hydrogen is introduced into the system, and the specimen heated until a pressure decrease corrected for temperature equivalent to the loading target is achieved. Remaining hydrogen is subsequently evacuated and replaced with ~800 Torr of helium. The specimen is then cooled slowly and stored until retrieved for use. Loading is evaluated by a change in mass.

2.2 Mechanical Testing

Mechanical testing of the specimens consisted of both hardness testing and tensile testing. The procedures are outlined below.

2.2.1 Tensile Testing

The fixturing for the tensile tests is shown in Figure 2-1, as are the nominal dog-bone sample dimensions:

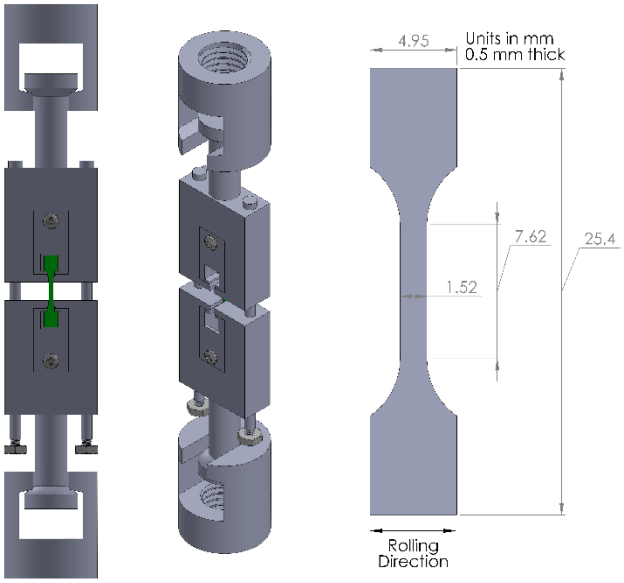

Figure 2-1: CAD renderings of tensile grips and nominal geometry of tensile specimens. An example of the tensile specimen inserted into the apparatus is highlighted in green in the left-hand section of the image.

This fixturing setup features a shoulder-loaded arrangement as opposed to the more traditional pin-loaded arrangement. The shoulder-loaded setup is advantageous as it eliminates the possibility of shear-out commonly seen in a pin-loaded setup as well as increasing the rigidity of the load train; the more rigid the load train, the more accurate the strain estimates of the tensile specimen will be since they were not measured directly in these experiments.

The samples were tested at room temperature using an Instron 5582 servo-mechanical test frame. While this study aims to reproduce the results of the study outlined in Li et al., the paper based on that study did not list the strain rate or geometry of the specimens [Li 2017]. As we are trying to recreate the results of that study in part of this effort, we were required to devise our own sample geometry and mechanical testing method, which may be different than that used in the previous study.

The tensile sample geometry shown on the right in Figure 2-1 is a commonly used tensile sample geometry for nuclear applications and has been widely and successfully used in the characterization of nuclear-grade stainless steels; while zirconium and steel alloys are highly different, this was a logical experimental base.

According to the work of Li et al., the samples tested were oriented in the transverse direction i.e. the direction in which the raw material sheets were rolled were oriented 90° to the longitudinal direction of the dog-bone specimen [Li 2017]. Accordingly, the samples in this study were machined in the same orientation from the vendor-supplied sheet. An extremely slow strain rate was desired for these specimens, but since strain was not controlled directly during these experiments these samples were loaded at a very slow displacement rate instead. The displacement resolution of the Instron 5582 is approximately 0.05 microns, so the displacement rate was set at 0.1 microns/s in order to reliably capture accurate displacement data.

An extremely slow strain rate was desired because at high displacement rates the crystallographic structure of the Zircaloy cannot deform in response but will rather fracture at low strains as though brittle. The $\delta - \zeta$ transformation of the brittle hydride phases of this material is contingent on the strain of the surrounding ductile matrix initiating the strain on the brittle phase. However, if the ductile phase is deformed too quickly, it will assume a pseudo-brittle behavior and not exert the necessary strain on the brittle phase to transform it to a more ductile zirconium-hydride phase.

2.2.2 Hardness Mapping

Atomic force microscopy analysis was carried out on an MFP-3D Infinity (Asylum/Oxford). Lateral force microscopy measurements were performed using a silicon nitride probe (Bruker, 0.03 N/m spring constant) with a set point of 1 V, and a scan speed of 1 Hz. Force mapping was carried out using a custom diamond probe (Micro Star Technologies, 100 N/m spring constant) with a set point of 50 µN. Hardness mapping was performed using a diamond probe with a sapphire cantilever (100 N/m spring constant, Micro Star Technologies, USA) with a set point of 5 to 10 µN.

2.3 Microscopy

To prepare samples for microscopic analysis, they were first sanded in increments to 320 grit sandpaper. Then samples were polished with 9 μm diamond, followed by 3 μm diamond. To remove polishing damage the samples were wiped with cotton swabs dipped in B-etch solution (mixture of 45 mL water, 45 mL HNO_3, and 10 mL HF). To finish the samples were placed on a vibratory polisher overnight in 0.05 μm colloidal silica suspension.

Scanning electron microscopy (SEM) was performed using a JEOL7600F field emission SEM equipped with an Oxford Instruments Symmetry electron backscatter diffraction (EBSD) CMOS detector. Specimen preparation utilized traditional metallographic grinding and polishing techniques to a final surface finish of 0.05 µm using colloidal silica media on a vibratory polisher. Following polishing, samples were carbon coated to ~6 nm. Data acquisition and analysis was performed using the Oxford Instruments AZtec Nanoanalysis software package (v4.1-4.3) along with the HKL Channel 5 and AZtec Crystal EBSD analysis software. Mapping was accomplished using an accelerating voltage of 20 kV, a probe current setting of 16, a working distance of ~24 mm and a specimen tilt of 70°. EBSD measurements were carried out a varied magnification ranging from 250X to 4000X, with step sizes ranging from 0.05 µm to 1.0 µm (depending on magnification). Indexed phases and their respective parameters are shown in Table 2-1 below. A medium level of data cleaning was performed close to unindexed regions along grain boundaries.

Table 2-1: Indexing information for phases in EBSD scans.

Phase	Structure	Laue Group	Space Group	Unit Cell (a,b,c)	Unit Cell (α,β,γ)
Zr	Hexagonal	9 (6/mmm)	194 (P 6_3/mmc)	a=b=3.2312, c=5.1477	90°,90°,120°
ZrH	Tetragonal	4(4/m)	86 (P 4_2/n)	a=b=4.5860, c=4.9840	90°,90°,90°
ZrH_2	Cubic	11 (m-3m)	225 (F m-3m)	a=b=c=4.7770	90°,90°,90°

2.4 Phase Field Modeling

In the phase field model, we considered three phases in the Zr-H system; α-Zr, γ-ZrH, and δ-$ZrH_{1.5+x}$. Each phase was controlled by a non-conserved order parameter η_α, η_γ, and η_δ. There was one eigenstrain variant of the γ phase included in each simulation to reduce the complexity of the model and minimize computation time. The Grand Potential (GP) model developed originally by Plapp [Plapp 2011] and adapted to a multiphase system by Aagesen et al. [Aagesen 2018] was used to simulate the evolution of the chemical potential. A recent work by Simon et al. describes the methods for adding elastic energy to the GP model; in this case the Khachaturian method described in that work was used [Simon 2020]. The total GP of the system is defined by:

$$\Omega = \int_V (\omega_{mw} + \omega_{grad} + \omega_{chem} + \omega_{elastic}) dV \quad (1)$$

where ω_{mw} is a multiwell function contributing to the bulk free energy, ω_{grad} is the gradient energy contribution, ω_{chem} is the chemical contribution, and $\omega_{elastic}$ is the elastic energy contribution following Khachaturyan's method. These terms are defined by the following equations:

$$\omega_{mw} = m_{ij} f_0 \quad (2)$$

$$f_0 = \sum_{i=1}^{N} \left(\frac{\eta_i^4}{4} - \frac{\eta_i^2}{2} \right) + \sum_{i=1}^{N} \sum_{j=1, j \neq i}^{N} \left(\frac{\gamma}{2} \eta_i^2 \eta_j^2 \right) + \frac{1}{4} \quad (3)$$

$$\omega_{grad} = \frac{\kappa_{ij}}{2} \sum_{i=1}^{N} |\nabla \eta_i|^2 \quad (4)$$

$$\omega_{chem} = \sum_{i=1}^{N} h_i \omega_i \quad (5)$$

$$\omega_{elastic} = \frac{1}{2} C_{ijkl} \varepsilon_{ij} \varepsilon_{kl} \quad (6)$$

Where m is a constant with units of energy density, i and j index the phases in the model, γ is 1.5 to create a symmetric interface between phases [Moelans 2008], η_i is the non-conserved order parameter for phase i, κ_{ij} is the gradient energy coefficient, N is the number of phases, h_i is a switching function for phase i, ω_i is the grand potential of phase i, C_{ijkl} is the elasticity and ε_{ij} is the local strain. The switching functions and grand potentials for each phase are as follows:

$$h_i = \frac{\eta_i^2}{\sum_{j=1}^{N} \eta_j^2} \tag{7}$$

$$\omega_i = f_{i,min} - \frac{1}{2}\frac{\mu^2}{V_a^2 A_i} - \frac{\mu}{V_a}\, c_{i,min} \tag{8}$$

Where μ is the chemical potential, V_a is the atomic volume determined by dividing the molar density by Avogadro's number, and A_i is the curvature of the parabola of the free energy for the given phase. This grand potential equation only applies for simple parabolic phase free energies of the form [Plapp 2011]:

$$f_i = f_{i,min} + \frac{1}{2}\, A_i \left(c - c_{i,min}\right)^2 \tag{9}$$

In this case the free energies of formation calculated by Christensen et al. for the Zr-H system were used for $f_{i,min}$, using $\alpha - Zr$ as the reference state [Christensen 2015]. The concentration as a function of chemical potential is also given by Aagesen et al as follows [Aagesen 2018]:

$$c = \sum_{i=1}^{N} h_i \left(\frac{\mu}{V_a A_i} + c_{i,min}\right) \tag{10}$$

Evolution of the non-conserved order parameters and the chemical potential are controlled by the Allen-Cahn equation and the general diffusion equation respectively:

$$\frac{\partial \eta_i}{\partial t} = -L\frac{\delta \Omega}{\delta \eta_i} \tag{11}$$

$$\chi \frac{\partial \mu}{\partial t} = \nabla \cdot M \nabla \mu - \frac{\partial \rho}{\partial \eta_i}\frac{\partial \eta_i}{\partial t} \tag{12}$$

where χ is the susceptibility, M is the mobility, and ρ is the density of hydrogen defined as follows [Plapp 2011]:

$$\chi = \frac{1}{V_a^2 A_i} \tag{13}$$

$$M = D\chi \tag{14}$$

$$\rho = \frac{\mu}{V_a^2 A_i} + \frac{c_{i,min}}{V_a} \tag{15}$$

The diffusion D is defined by Zhang et al [Zhang 2017].

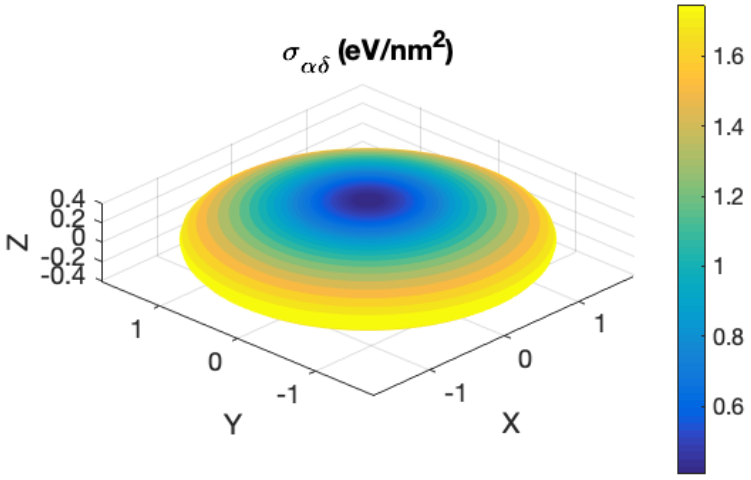

Figure 2-2: Interface energy between α and δ phases in units of $\frac{eV}{nm^2}$. Directions are $[11\bar{2}0]$, $[10\bar{1}0]$, and $[0001]$ for x, y and z respectively.

While previous models of Zr-H have used isotropic interface energies this model will use anisotropic interface energies created by modifying the γ_{ij} parameter to be anisotropic. The interface energy between two phases, σ_{ij}, for symmetrical interfaces is given by Moelans et al. as [Moelans 2008]:

$$\sigma_{ij} = \frac{1}{3}\sqrt{m\kappa\left(\frac{1}{2} + \gamma_{ij}\right)} \tag{16}$$

With this equation in mind and the anisotropic interface energies for $\alpha - \gamma$ and $\alpha - \delta$ phases given by Louchez et al. [Louchez 2017] and Han et al. [Han 2019] respectively, κ_{ij} is set to be an ellipsoid for both interfaces as follows:

$$\gamma_{ij} = \left(\frac{\sin^2\phi}{\gamma_{ij,prism}} + \frac{\cos^2\phi}{\gamma_{ij,basal}}\right)^{-\frac{1}{2}} \tag{17}$$

This is done to simplify the model with no knowledge of interface energies other than the basal and prismatic planes given in the cited sources. An example of the resulting interface energy from equation 16 for $\sigma_{\alpha\delta}$ is shown in Figure 2-2. All material properties and model parameters are given in Table 2-2 with references.

Table 2-2: Material properties used in simulations with references for each value. Values calculated from equations in this work are not given external references.

Property	Value	Ref	Property	Value	Ref	Property	Value	Ref
C_{11}^{α}	155 GPa	[Olsson 2014]	C_{11}^{γ}	122 GPa	[Olsson 2014]	C_{11}^{δ}	162 GPa	[Olsson 2014]
C_{12}^{α}	67 GPa	[Olsson 2014]	C_{12}^{γ}	116 GPa	[Olsson 2014]	C_{12}^{δ}	103 GPa	[Olsson 2014]
C_{13}^{α}	64 GPa	[Olsson 2014]	C_{13}^{γ}	98 GPa	[Olsson 2014]	C_{13}^{δ}	109 GPa	[Olsson 2014]
C_{33}^{α}	173 GPa	[Olsson 2014]	C_{33}^{γ}	183 GPa	[Olsson 2014]	C_{33}^{δ}	166 GPa	[Olsson 2014]
C_{44}^{α}	40 GPa	[Olsson 2014]	C_{44}^{γ}	47.5 GPa	[Olsson 2014]	C_{44}^{δ}	69.3 GPa	[Olsson 2014]
C_{66}^{α}	44 GPa	[Olsson 2014]	C_{66}^{γ}	61.1 GPa	[Olsson 2014]	C_{66}^{δ}	66.8 GPa	[Olsson 2014]
$\sigma_{\alpha\gamma,basal}$	$200\frac{mJ}{m^2}$	[Louchez 2017]	$\sigma_{\alpha\delta,basal}$	$65\frac{mJ}{m^2}$	[Han 2019]	κ	$0.67\frac{mJ}{m^2}$	n/a
$\sigma_{\alpha\gamma,prism}$	$750\frac{mJ}{m^2}$	[Louchez 2017]	$\sigma_{\alpha\delta,prism}$	$280\frac{mJ}{m^2}$	[Han 2019]	m	1.5	n/a
$\gamma_{\alpha\gamma,basal}$	13.5	n/a	$\gamma_{\alpha\delta,basal}$	1	n/a	L	$10 * M$	n/a
$\gamma_{\alpha\gamma,prism}$	195	n/a	$\gamma_{\alpha\delta,prism}$	27	n/a			n/a
$\varepsilon_{11}^{\gamma,sf}$	0.00551	[Bair 2017]	$\boldsymbol{\varepsilon_{11}^{\delta,sf}}$	0.0458	[Bair 2017]			
$\varepsilon_{22}^{\gamma,sf}$	0.0564	[Bair 2017]	$\boldsymbol{\varepsilon_{22}^{\delta,sf}}$	0.0458	[Bair 2017]			
$\varepsilon_{33}^{\gamma,sf}$	0.057	[Bair 2017]	$\boldsymbol{\varepsilon_{33}^{\delta,sf}}$	0.072	[Bair 2017]			

3.0 Results and Discussion

3.1 Phase field modeling

Phase field models of a zirconium-hydrogen system (1 at% hydrogen) with two seed grains, one of delta-phase hydride and one of gamma-phase hydrides in zirconium, were performed under conditions of zero stress and under 300 MPa of uniaxial stress. The results of these models are portrayed in Figure 3-1 and Figure 3-2, respectively. In applied stress case, the stress is applied in the direction perpendicular to the original grain growth, to simulate strain applied transverse to the rolled direction.

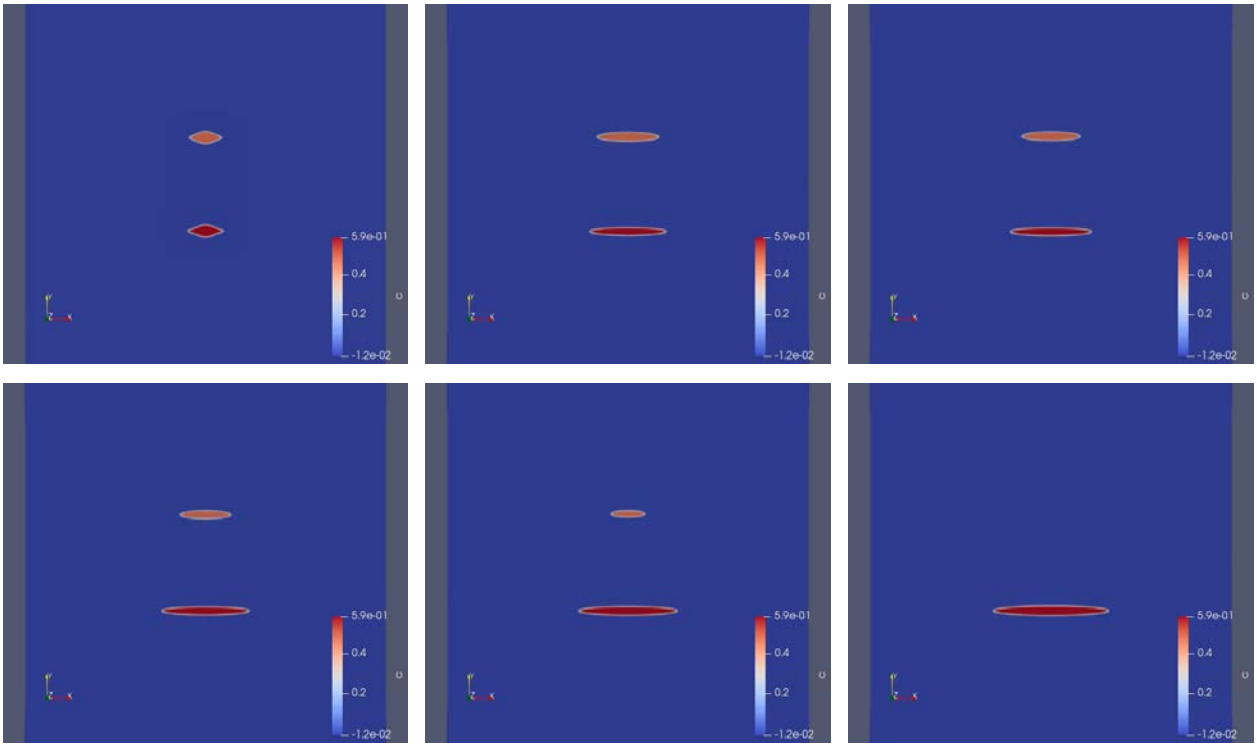

Figure 3-1: Progression of phase field modeling of the unstressed hydride formation. While both gamma zirconium hydride (pink) and delta zirconium hydride (red) form initially, the more stable delta zirconium hydride begins to grow at the expense of the gamma hydride about half-way through, ultimately completely eliminating it.

In the case of the unstressed system, the expected progression occurs. Both hydrides grow from their seeds while free hydrogen is plentiful in the system. Once the free hydrogen is consumed, the delta hydride continues to grow at the expense of the gamma hydride, which shrinks as its hydrogen is transferred to the growing delta hydride grain. Eventually, the gamma hydride vanishes, leaving behind the delta hydride grain.

In the case with applied stress, a different scenario is predicted. While both grains again initially grow while free hydrogen is available, the gamma hydride grows to align perpendicular the applied stress, while the delta hydride is deformed but remains largely in line with the applied stress, growing in the same direction it did without any stress applied. The gamma hydride eventually grows into the delta hydride and absorbs it, leaving behind a gamma hydride perpendicular to the direction of the stress.

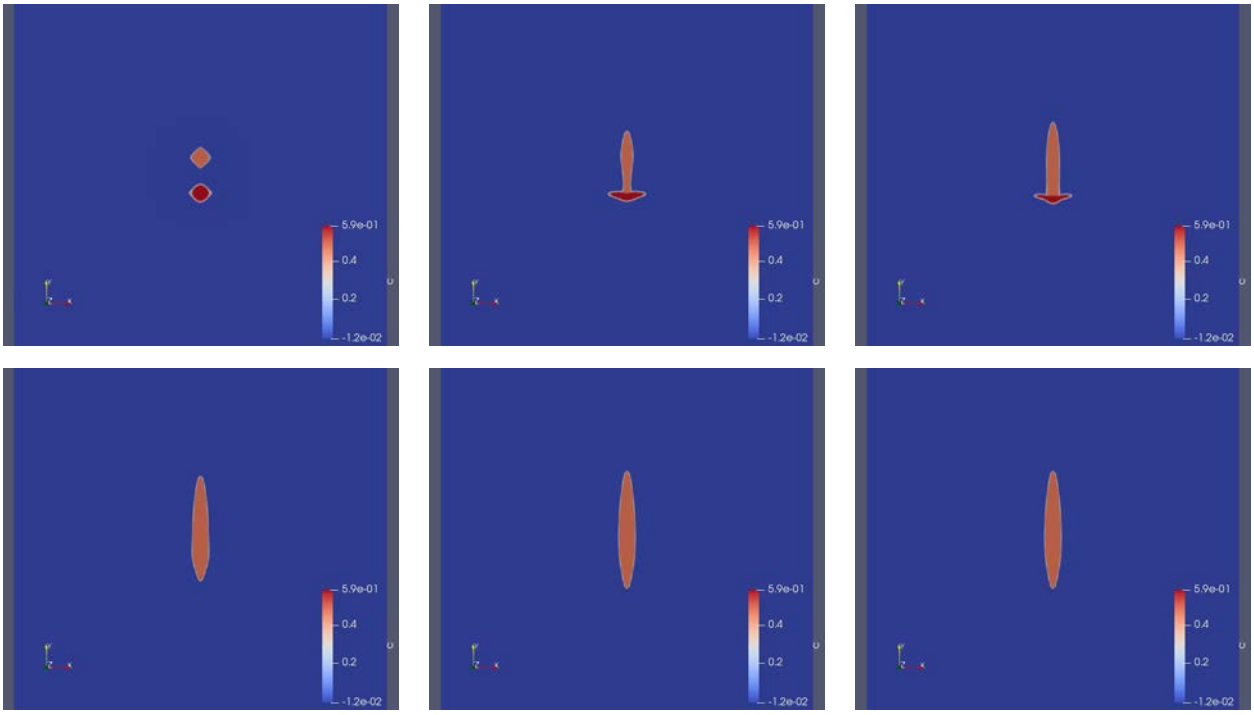

Figure 3-2: Progression of phase field modeling of the hydrides, starting from the same seeds, with 300 MPa of uniaxially applied stress in the x-direction (horizontally). Again, both gamma zirconium hydride (pink) and delta zirconium hydride (red) initially form. However, with the applied stress, the gamma zirconium hydride is predicted to be more stable and grows aligned perpendicular with the stress, while the delta hydride grows parallel to the stress. The gamma hydride absorbs the delta hydride after contacting it, leaving behind the single gamma hydride aligned perpendicular to the stress direction.

Initial experimental tests of applying stress to hydrided zirconium metal did not reproduce the results of the phase field models. One explanation for this discrepancy may lie in the free energies used to construct the model, as shown in Figure 3-3. For consistency, the bulk free energy for the gamma and delta phases were both taken from Christensen et al. for the phase field model performed here. However, the data reported by Dupin, derived from experimental data versus Christensen et al.'s DFT simulations, reports a much lower, and thus more stable, free energy for the delta phase [Dupin 1999, Christensen 2015]. Dupin unfortunately does not report a free energy for the gamma phase. Because of this conflict, the remainder of the project focused on understanding the conditions required to replicate the results of Li et al. [Li 2017].

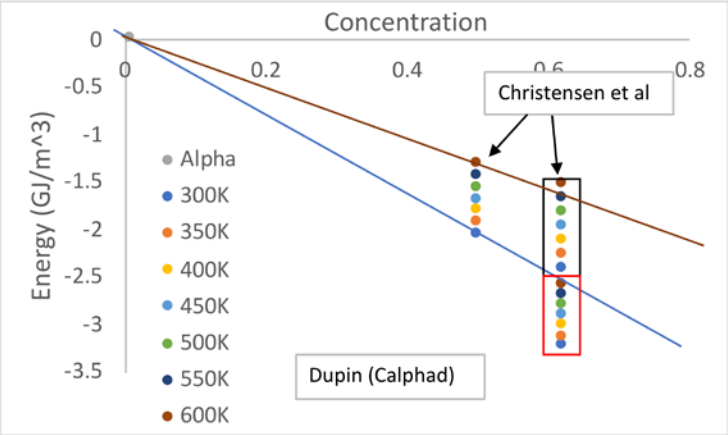

Figure 3-3: Bulk free energy of the gamma (left row of dots) and the delta (right row of dots) hydride phases relative to alpha zirconium at different temperatures, as a function of their hydrogen concentrations. Discrepancies between Christensen's DFT simulation data for the delta hydride and the Calphad data from Dupin are evident.

3.2 Tensile Measurements

Figure 3-4 shows the stress-strain curves for the unhydrided Zircaloy-4 tested in the transverse direction. The sample numbers and hydrogen loading levels are listed in the legend of the figure. These results are typical for Zircaloy-4 in transverse rolling, with ultimate strength values of approximately 550-600 MPa. There is a noticeable variation between the tensile curves of each specimen, but this is common among rolled material tested in the transverse direction; the differences are not extreme, so any differences between the curves are purely statistical.

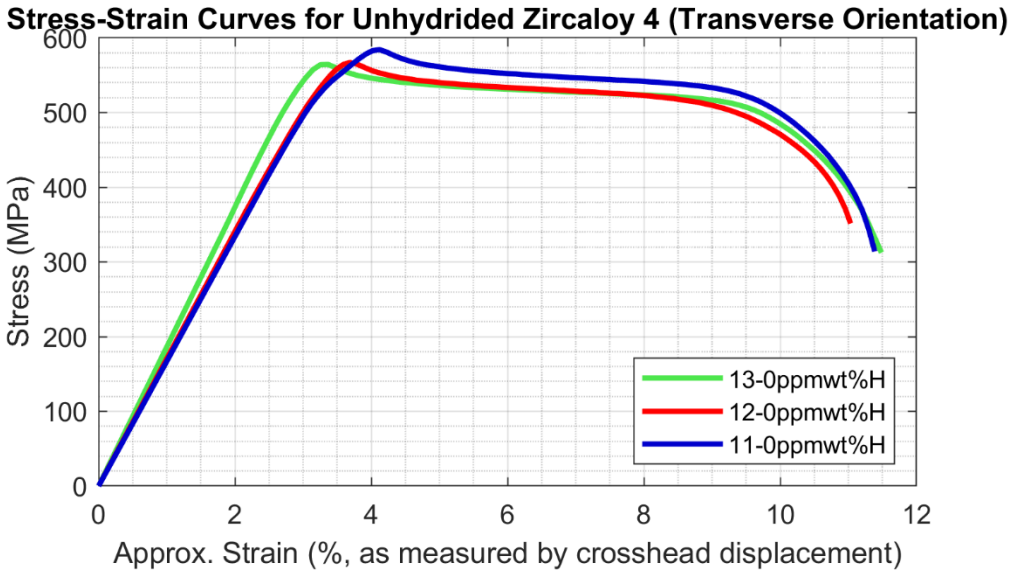

Figure 3-4: Stress-strain curves for unhydrided transverse-oriented Zircaloy-4.

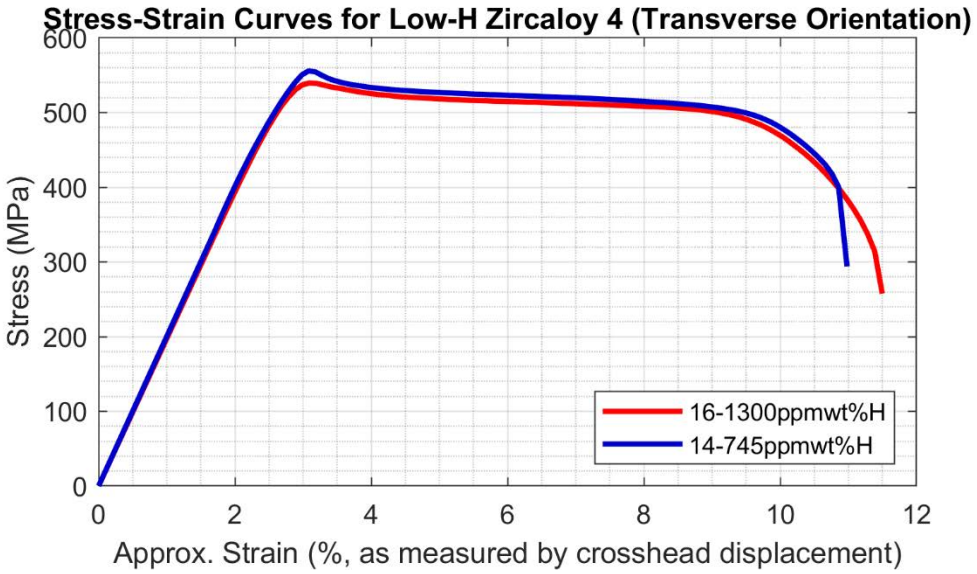

Figure 3-5: Stress-strain curves for low-H transverse-oriented Zircaloy-4.

Figure 3-5 shows the stress-strain curves for the low-hydrided Zircaloy-4 specimens. Though these specimens were hydrided and therefore embrittled to an extent, their mechanical behavior under tensile load is almost identical to that of the unhydrided specimens. This is an important result, as it shows that not only can Zircaloy-4 withstand mild hydriding and maintain its ductility, but that the procedure outlined in Li et al., though contradictory to a certain extent based on these results, is still feasible [Li 2017]. If these mildly-hydrided specimens had shown behavior similar to the highly hydrided specimens (shown in Figure 3-6 below), then the concept of using mechanical stress to initiate a brittle-ductile transition of the brittle hydride phases of this material would be completely invalid from a practical standpoint, as the brittle phases require ductile deformation of the surrounding matrix to transfer the force to them locally and achieve ductility themselves. However, as these materials have shown to retain ductility not only at the loadings presented in Li et al., but in loadings that exceed them, then with the proper application of mechanical stress it is feasible that the delta-gamma transformation explored in the previous study may be achieved [Li 2017].

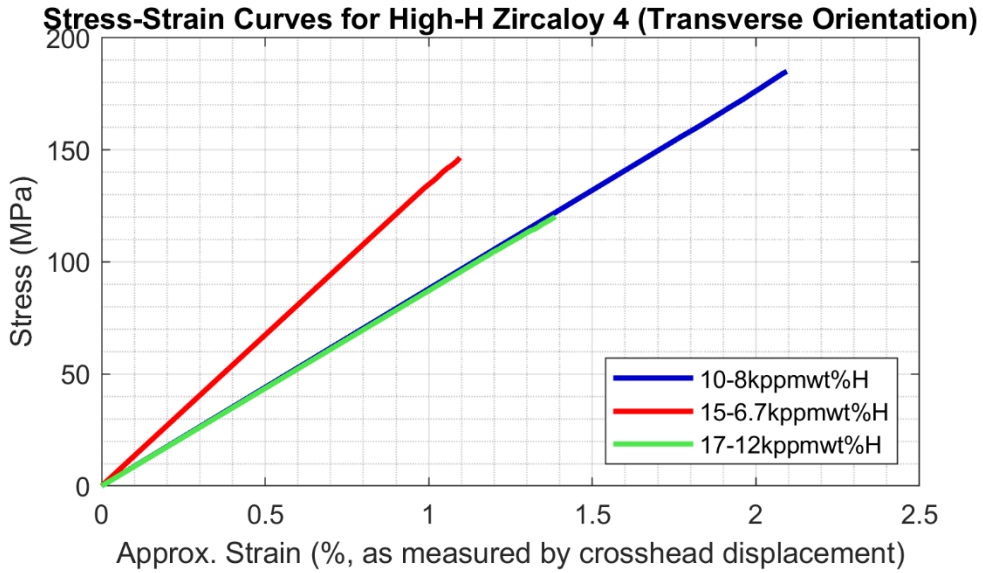

Figure 3-6: Stress-strain curves for high-H transverse-oriented Zircaloy-4.

Figure 3-6 shows the stress-strain curves for the highly-hydrided samples. In the study by Li et al., the zircaloy was hydrided to approximately 600 ppm by weight hydrogen [Li 2017]. These tests aimed to explore the effects of hydriding to comparable levels but also to considerably more extreme levels, in this case approximately one order of magnitude higher concentration. As shown in Figure 3-6, both the strength and ductility of the Zircaloy-4 decreases by an extreme amount after high-level hydriding. This observation is somewhat counterintuitive to what would be expected, as factors that lead to decreases in ductility often lead to increases in strength, because precipitation of new phases, in small amounts, prevents defect migration and interferes with crack propagation. However, it is also known that for materials susceptible to hydriding that the hydrogen tends to bond to the metal elements at the grain boundaries, leading to intergranular embrittlement and weakness. This effect would be especially pronounced in the transverse orientation, where the boundaries between grains generally lie perpendicular to the direction of the applied load and are therefore especially weak. Large numbers of included precipitates can also interrupt the matrix and be a nucleation site for crack formation and propagation, as is seen in carbide precipitates in uranium [Davies 1961].

3.3 Hardness Measurements

AFM based force mapping reveals the distribution of hardness across the hydrided Zircaloy-4 surface. The slight variation of hardness between grains, likely due to crystal orientation, allows for the visualization of individual grains that are not as apparent in the surface morphology. This variation between grains is more pronounced in sample ZrH#15 (6700 ppm hydrogen) than in the 5 at. % no stress sample (8000 ppm hydrogen) as shown in Figure 3-7. The hydride identified as the ZrH_2 phase by EBSD is approximately 26 % (5 at. % no stress) and 35% (ZrH #15) harder than the surrounding Zircaloy-4. The needlelike hydride phase both cuts through individual Zircaloy-4 grains and resides within grain boundaries.

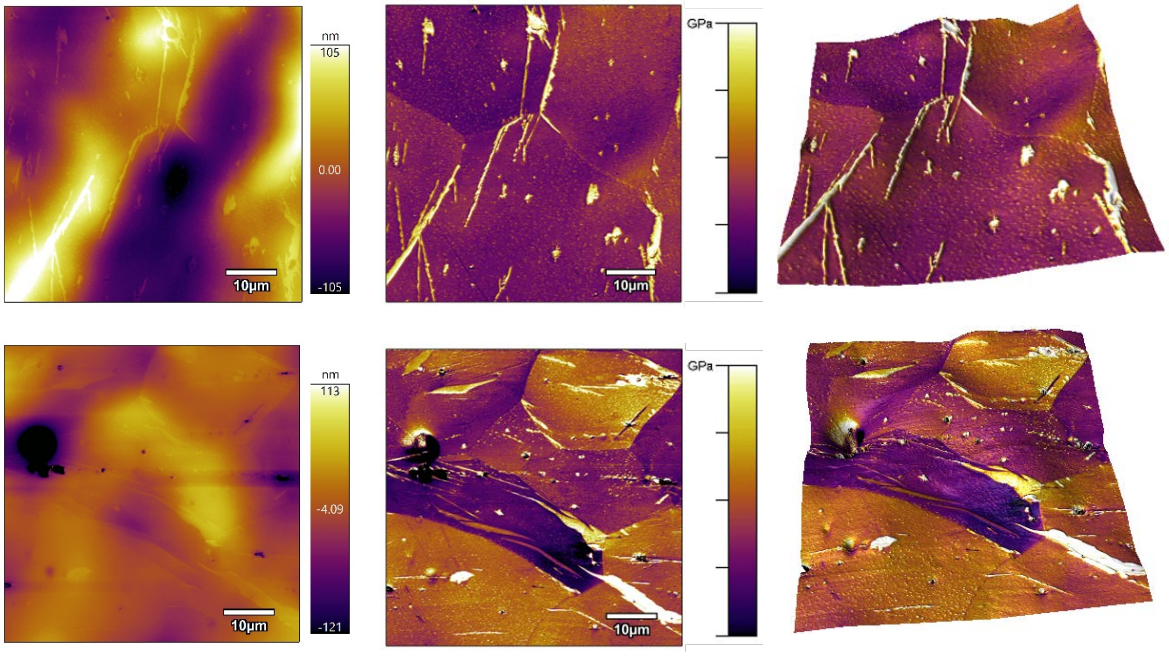

Figure 3-7: Topography, relative hardness and 3D projection overlay of the 5 at. % no stress sample (top) and ZrH #15 sample (bottom) surface. 512 x 512 force curves were taken approximately every 117 nm with a setpoint of 10 µN.

3.4 Microscopy

In order to assess and determine microstructural features associated with hydride formation in Zr-based material, hydrogen charging to an extreme degree was performed. Figure 3-8 shows back-scattered electron (BSE) images that reveal hydride formation is comprised of both banding and needle-like morphologies that extend through grain interiors in a linear fashion. Growth of hydrides appears inhibited by the presence of grain and/or sub-grain boundaries. This is visualized in the form of clear changes in the hydride alignment that coincide with BSE grain contrast at boundaries.

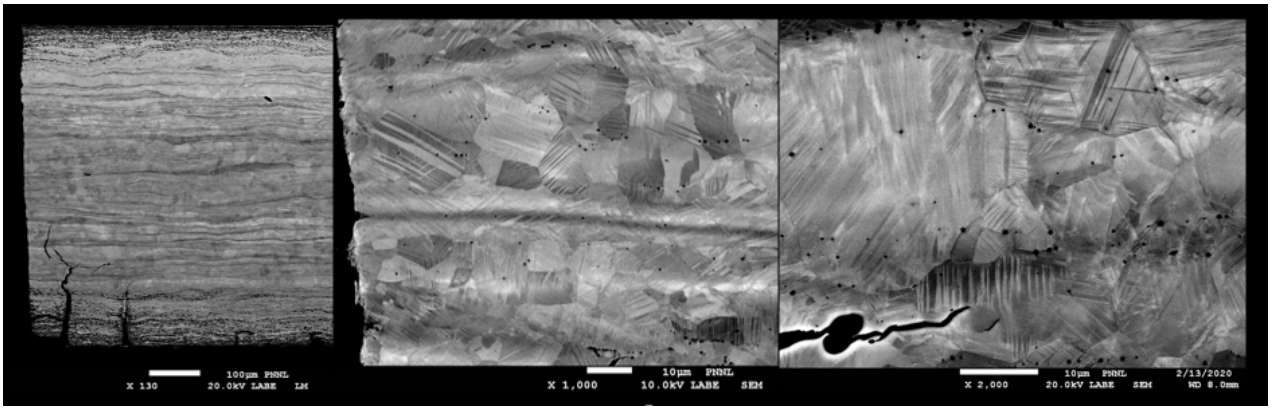

Figure 3-8: Backscattered electron images taken at successively higher magnification of a heavily hydrided material to visualize the effect of hydride formation on the Zr microstructure.

Scanning electron microscopy coupled with EBSD mapping was then performed on unstrained Zircaloy-4 material after hydrogen charging to 5 at.%, as shown in Figure 3-9. These results revealed that at 5 at.% charging, significant hydride formation was present along the material surface. This hydride formation extended from the surface towards the specimen interior roughly 50 µm. A large number of δ-hydrides are observed, with a lower volume fraction of interspersed γ-hydrides. Alignment of these needle-like hydrides appears to coincide with the exterior surface of the specimen, such that the long axis is parallel to the exterior surface. The hydride thickness also appears to decrease away from the exterior surface of the material. At locations further from the specimen surface, alignment of the long axis of the hydrides appears more varied, and extends to grain interiors from grain boundary triple points. This is likely a result of increased H diffusivity along grain boundaries and their junctions. Inspection of the IPF-X,Y and Z maps indicates that hydride growth exhibits preferred orientation dependence.

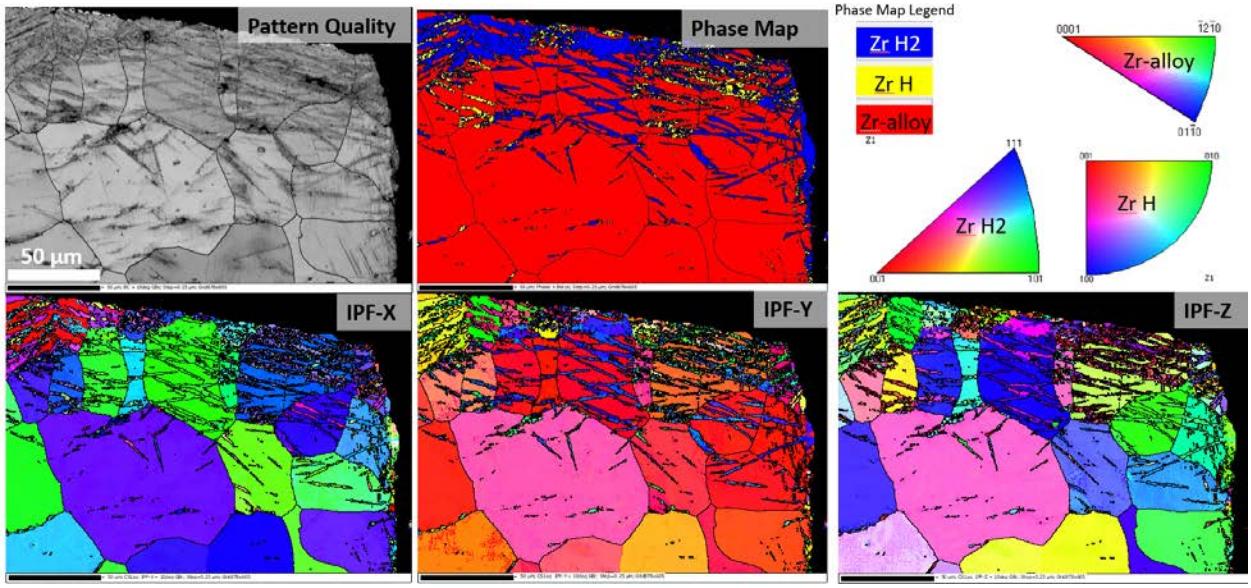

Figure 3-9: SEM microscopy and EBSD patterns of Zirconium-4 alloy hydrided to 5 at%. The patterns shows strong formation of the delta phase (ZrH_2) at the surface, with minor inclusion of gamma phase (ZrH). Grains of the hydrided phases are largely intergranular and not associated with the grain boundaries of the underlying structure.

Images from the same alloy after stressing to failure are shown in Figure 3-11. No significant transformation of the δ-hydrides is to γ-hydrides is observed, and the overall proportion of the hydrides remains the same. The hydrides remain in similar alignment to the surface and no dramatic orientation shifts are visible following applied strain.

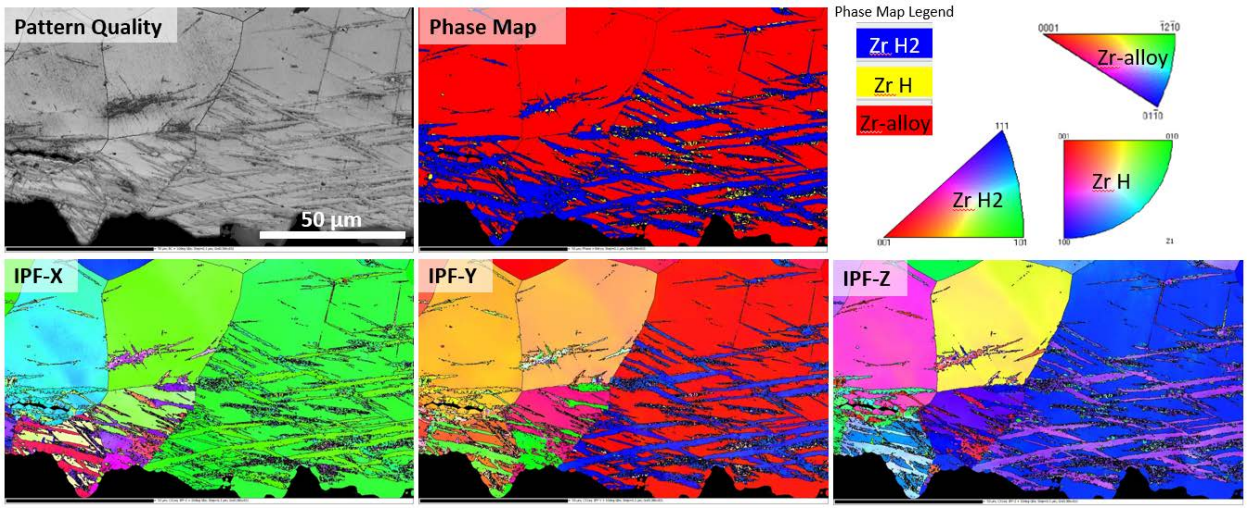

Figure 3-10: EBSD maps of 5 at. % hydrided zircaloy-4 stressed to fracture at 430 MPa. No significant change in the proportion of delta and gamma phase hydrides is observed after stress was applied.

Higher resolution EBSD mapping was performed on this specimen to ensure that refined γ-hydrides were not present, but beyond the length scale of the initial EBSD scans. Results of higher resolution mapping are shown in Figure 3-11. The region of interest selected for high resolution mapping is indicated by the yellow callout. This region was selected because weak γ-hydride formation was observed in the initial scans. High resolution mapping did not reveal a significant increase in the fraction of γ-hydride present in this region.

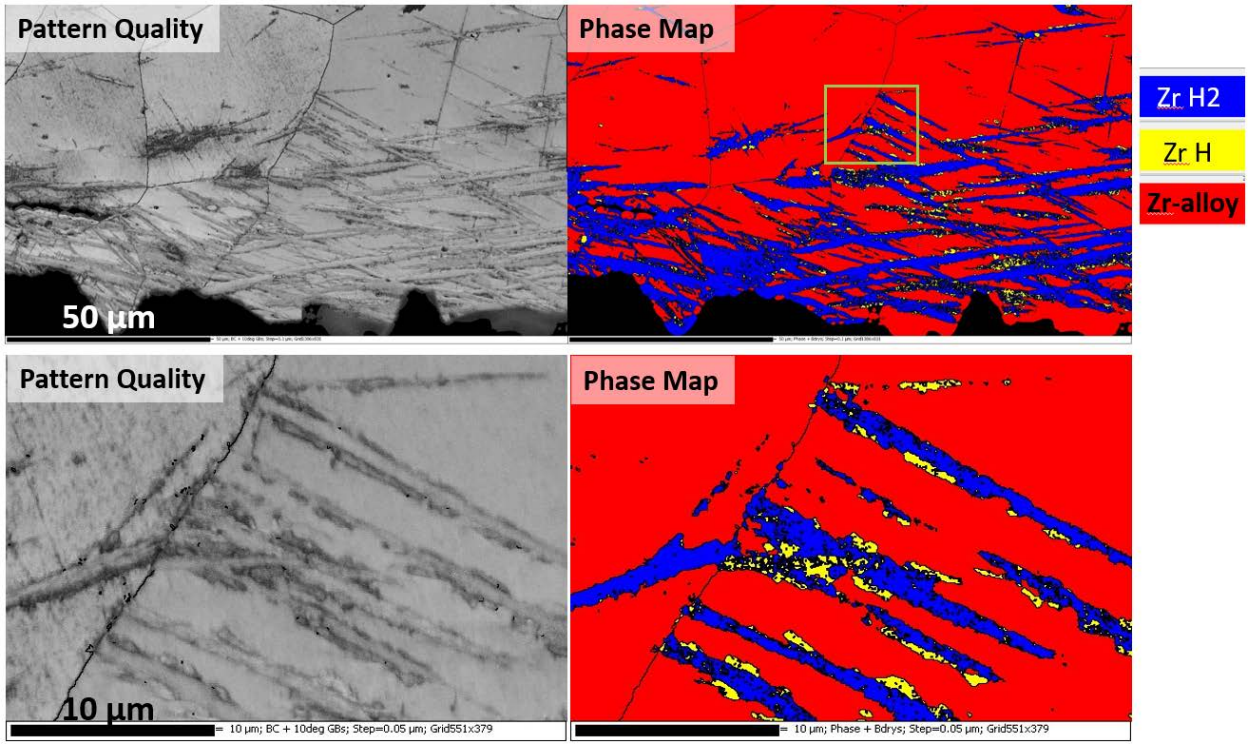

Figure 3-11: Low and high resolution comparison of EBSD maps from the 5 at. % hydride zircaloy-4 specimen stressed to fracture at 430 MPa. No significant change in the proportion of delta and gamma phase hydrides is observed after stress was applied.

These results suggest that a delta to gamma hydride transformation does not occur in H-charged zircaloy metal that later undergoes tensile stress. This does not completely replicate the results of Li et al, who performed hydriding at the same time that the system was being stressed [Li 2017]. This points to the δ-hydride to γ-hydride transition being difficult to achieve, and the need to form the γ-hydrides in situ if they are to be a major component of the zircaloy and contribute to the ductility of the material.

4.0 Conclusions

Through the course of this work, we were not able to replicate previous results claiming to stabilize the γ-zirconium hydride phase through mechanical stress [Li 2017]. We saw extensive formation of δ-hydrides at the surface of the hydrided material, as both intergranular and intragranular inclusions. The difficulty in replicating the previous study may have been in our ability to only stress the material after the material was already hydrided, rather than in situ during formation of the hydrides. This points to the δ-hydride to γ-hydride transition being relatively difficult to achieve, and the need to form γ-hydrides directly while the material is under stress if they are to be included in a strategy to maintain ductility in nuclear cladding material.

5.0 References

[Aagesen 2018] Aagesen, L. K., and Y. Gao, D. Schwen, K. Ahmed. 2018. Grand-potential-based phase-field model for multiple phases, grains, and chemical components, Phys. Rev. E. 98, p. 023309. doi:10.1103/PhysRevE.98.023309.

[Bair 2015] Bair, J. L., and M. Asle Zaeem, M.R. Tonks. 2015. A Review on Hydride Precipitation in Zirconium Alloys, J. Nucl. Mater. 466, pp. 12–20. doi:10.1016/j.jnucmat.2015.07.014.

[Bair 2016] Bair, J.L. 2016. Multiphase field modeling of the formation path of delta hydrides in zirconium. Missouri University of Science and Technology doctoral thesis. https://scholarsmine.mst.edu/doctoral_dissertations/2527/ (Accessed 9/21/2020).

[Bair 2017] Bair, J. L., and M. Asle Zaeem, D. Schwen. 2017. Formation path of δ-hydrides in zirconium by multiphase field modeling, Acta Mater. 123, pp. 235–244. doi:10.1016/j.actamat.2016.10.056.

[Chernov 2017] Chernov, I. I., and M.S. Staltsov, B.A. Kalin, L.Y. Guseva. 2017. Some problems of hydrogen in reactor structural materials: A review, Inorg. Mater. Appl. Res. 8, pp. 643–650. doi:10.1134/S2075113317050094.

[Christensen 2015] Christensen, M., and W. Wolf, C. Freeman, E. Wimmer, R.B. Adamson, L. Hallstadius, P.E. Cantonwine, E. V Mader. 2015. H in α-Zr and in zirconium hydrides: solubility, effect on dimensional changes, and the role of defects., J. Phys. Condens. Matter. 27, p. 025402. doi:10.1088/0953-8984/27/2/025402.

[Cox 1990] Cox, B. 1990. Environmentally-induced cracking of zirconium alloys - A review, J. Nucl. Mater. 170, pp. 1–23. doi:10.1016/0022-3115(90)90321-D.

[Davies 1961] Davies, D. M. and J. W. Martin. (1961). The Effect of Inclusions on the Fracture of Uranium. J. Nucl. Mater. 3, pp. 156-161.

[Dupin 1999] Dupin, N. and I. Ansara, C. Servant, C. Toffolon, C. Lemaignan, J. C. Brachet.1999. A thermodynamic database for zirconium alloys. J. Nucl. Mater. 275, pp. 287-295. doi:10.1016/S0022-3115(99)00125-7.

[Ells 1968] C.E. Ells, C. E. 1968. Hydride precipitates in zirconium alloys (A review), J. Nucl. Mater. 28, pp. 129–151. doi:10.1016/0022-3115(68)90021-4.

[Ensor 2017] Ensor, B. and A.M. Lucente, M.J. Frederick, J. Sutliff, A.T. Motta. 2017. The role of hydrogen in zirconium alloy corrosion, J. Nucl. Mater. 496, pp. 301–312. doi:10.1016/j.jnucmat.2017.08.046.

[Han 2019] Han, G. M., and Y.F. Zhao, C.B. Zhou, D. Lin, X.Y. Zhu, J. Zhang, S.Y. Hu, H.F. Song. 2019. Phase-field modeling of stacking structure formation and transition of d-hydride precipitates in zirconium, Acta Mater. 165, pp. 528–546. doi:10.1016/j.actamat.2018.12.009.

[Li 2017] Li, S., and Y. Wang, Z. Che, G. Liu, Y. Ren, Y. Wang. 2017. Investigations of deformation-induced δ → ζ phase transformation in zirconium hydride by in situ high-energy X-ray diffraction, Acta Mater. 140, pp. 168–175. doi:10.1016/j.actamat.2017.08.047.

[Louchez 2017] Louchez, M.-A., and R. Besson, L. Thuinet, A. Legris. 2017. Interfacial properties of hydrides in α -Zr: a theoretical study, J. Phys. Condens. Matter. 29, p. 415001. doi:10.1088/1361-648X/aa7f8a.

[Moelans 2008] Moelans, N., and B. Blanpain, P. Wollants. 2008. Quantitative analysis of grain boundary properties in a generalized phase field model for grain growth in anisotropic systems, Phys. Rev. B - Condens. Matter Mater. Phys. 78, p. 024113. doi:10.1103/PhysRevB.78.024113.

[Olsson 2014] Olsson, P. A. T., and A.R. Massih, J. Blomqvist, A.M. Alvarez Holston, C. Bjerken. 2014. Ab initio thermodynamics of zirconium hydrides and deuterides, Comput. Mater. Sci. 86, pp. 211–222. doi:10.1016/j.commatsci.2014.01.043.

[Plapp 2011] Plapp, M. 2011. Unified derivation of phase-field models for alloy solidification from a grand-potential functional, Phys. Rev. E - Stat. Nonlinear, Soft Matter Phys. 84, p. 031601. doi:10.1103/PhysRevE.84.031601.

[Simon 2020] Simon, P.-C. A., and L.K. Aagesen, A.T. Motta, M.R. Tonks. 2020. The effects of introducing elasticity using different interpolation schemes to the grand potential phase field model, Comput. Mater. Sci. 183, p. 109790. doi:10.1016/j.commatsci.2020.109790.

[Wang 2016] Wang, Z., and A. Steuwer, N. Liu, T. Maimaitiyili, M. Avdeev, J. Blomqvist, C. Bjerkén, C. Curfs, J.A. Kimpton, J.E. Daniels. 2016. Observations of temperature stability of γ-zirconium hydride by high-resolution neutron powder diffraction, J. Alloys Compd. 661, pp. 55–61. doi:10.1016/j.jallcom.2015.11.187.

[Zhang 2017] Zhang, Y., and C. Jiang, X.M. Bai, Anisotropic hydrogen diffusion in α -Zr and Zircaloy predicted by accelerated kinetic Monte Carlo simulations, Sci. Rep. 7, pp. 1–13. doi:10.1038/srep41033.

[Zhu 2010] Zhu, W., and R. Wang, G. Shu, P. Wu, H. Xiao. 2010. First-principles study of different polymorphs of crystalline zirconium hydride, J. Phys. Chem. C. 114, pp. 22361–22368. doi:10.1021/jp109185n.

Pacific Northwest National Laboratory

902 Battelle Boulevard
P.O. Box 999
Richland, WA 99354
1-888-375-PNNL (7665)

www.pnnl.gov